

## An automated pipeline for mitochondrial segmentation on ATUM-SEM stacks

Weifu Li<sup>\*,†</sup>, Hao Deng<sup>‡,§</sup>, Qiang Rao<sup>†</sup>, Qiwei Xie<sup>†,||,††</sup>,  
Xi Chen<sup>†</sup> and Hua Han<sup>†,§,¶,\*\*††</sup>

<sup>\*</sup>*Faculty of Mathematics and Statistics  
Hubei University, Wuhan 430062, China*

<sup>†</sup>*Institute of Automation, Chinese Academy of Sciences  
Beijing 100190, China*

<sup>‡</sup>*Faculty of Information Technology, Macau  
University of Science and Technology  
Macau 999078, China*

<sup>§</sup>*Future Technological College  
University of Chinese Academy of Sciences  
Beijing 100190, China*

<sup>¶</sup>*CBS Center for Excellence in Brain Science  
and Intelligence Technology  
Shanghai 200031, China  
lqiwei.xie@ia.ac.cn  
\*\*hua.han@ia.ac.cn*

Received 2 November 2016

Accepted 10 May 2017

Published 14 June 2017

It is possible now to look more closely into mitochondrial physical structures due to the rapid development of electron microscope (EM). Mitochondrial physical structures play important roles in both cellular physiology and neuronal functions. Unfortunately, the segmentation of mitochondria from EM images has proven to be a difficult and challenging task, due to the presence of various subcellular structures, as well as image distortions in the sophisticated background. Although the current state-of-the-art algorithms have achieved some promising results, they have demonstrated poor performances on these mitochondria which are in close proximity to vesicles or various membranes. In order to overcome these limitations, this study proposes explicitly modelling the mitochondrial double membrane structures, and acquiring the image edges by way of ridge detection rather than by image gradient. In addition, this study also utilizes group-similarity in context to further optimize the local misleading segmentation. Then, the experimental results determined from the images acquired by automated tape-collecting ultramicrotome scanning electron microscopy (ATUM-SEM) demonstrate the effectiveness of this study's proposed algorithm.

**Keywords:** ATUM-SEM; membrane enhancement; mitochondria; group-similarity.

†† Corresponding authors.

## 1. Introduction

At the current time, there is no doubt that mitochondria are the most essential and versatile organelle in a majority of eukaryotic cells. They carry out all types of important cellular functions including producing the overwhelming majority of cellular ATP needed for endoergic processes, and also regulating cytosolic  $\text{Ca}^{2+}$  transients.<sup>1</sup> Moreover, mitochondrial functions play a crucial role in the regulation of cellular life and death, including disease states. Disturbances in the mitochondrial functions and distribution can be accompanied by significant morphological alterations.<sup>2</sup> Consequently, many meaningful research studies have focused their investigations on the relationship between the mitochondrial locations and morphology, and the corresponding functions. A growing body of evidence has indicated that the mitochondrial distribution inside a cell can be strikingly heterogeneous.<sup>1</sup> For example, they are often enriched at the cellular sites where the demands for energy are greater, or where their metabolic functions are required, such as at the level of the synaptic bouton. Recent studies have shown that the regulation of mitochondrial shapes is crucial for cellular physiology, since changes in mitochondrial shapes have been linked to neurodegeneration, calcium signaling, lifespan, and cell death, which further expounds the crucial role that morphological changes of mitochondria play in the immune system.<sup>3</sup> Furthermore, it has been established that the function of mitochondria is closely related to cancer.<sup>4</sup> Some specific examples have demonstrated that the mitochondria in cancer cells can alter the function of resisting apoptosis,<sup>5,6</sup> which has naturally led the research studies regarding cancer therapy to focus on mitochondria by stimulating mitochondrial membrane permeability, or by changing the mitochondrial metabolism.<sup>7</sup> Along with the important role in physiological functions, mitochondria can also be regarded as the preferable corresponding landmarks across adjacent sections for image registration due to their homogeneous shapes and wide scatter.<sup>8</sup> This is the basis of 3D reconstruction from the electron microscopy (EM) images of serial sections, which is used in the analysis of the structures of biological specimens, such as the neuronal circuits in brain tissue.<sup>9,10</sup> Therefore, the automatic detection and segmentation of the mitochondria from intracellular space has been found to be very meaningful for cancer simulations and 3D reconstructions.

Mitochondrial shapes vary in living cells, and can range from punctuate structures to tubular networks, the sizes of which may vary between 0.3 and 10  $\mu\text{m}$ .<sup>11</sup> Optical microscopy with a limiting resolution cannot provide sufficient resolution to reveal these fine structures. Fortunately, recent progress has been made regarding super-resolution electronic microscopy, and it has already been possible to acquire images with higher resolutions, which have provided new penetrations into mitochondrial structures and functions.<sup>12</sup> In Fig. 1, the left picture depicts a biological specimen from a mouse cortex, and a region of interest (indicated by a red rectangle) is shown in the right picture. The data used in this study was acquired by automated

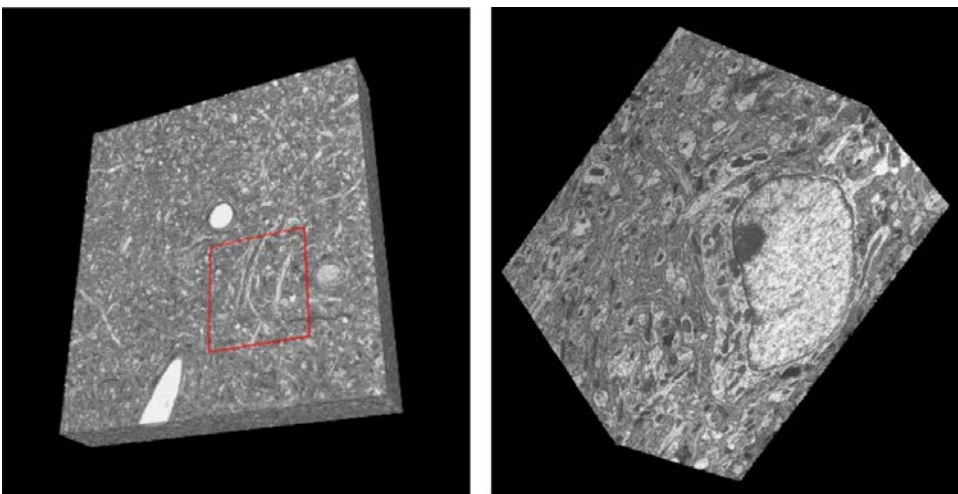


Fig. 1. Left: Tissue from a mouse cortex; Right: A region of interest indicated by a red rectangle.

tape-collecting ultramicrotome scanning electron microscopy (ATUM-SEM). Then, 178 sections with thicknesses of 50 nm were automatically cut and collected from a water bath using a custom designed tape-collection conveyor belt.<sup>13</sup> Since the support tape was electron opaque, the ATUM sections were mounted on an imaging plate, and imaged with SEM (Zeiss Supra55) at the Institute of Automation, CAS, where the pixel size was set at 2 nm. The EM images with higher resolution will inevitably produce more data at the same volume. The hand segmentation from the above image stack requires months of tedious manual labor. Also, considerable attention is paid to the automated data analysis which has greatly lagged behind the data acquisition. Nevertheless, the EM data has a sophisticated background, which violates the standard assumption that strong image gradient always corresponds to significant boundaries. The state-of-the-art algorithms are powerless on these mitochondria in close proximity to vesicles or various membranes.<sup>14,15</sup> In order to overcome this drawback, this study improves upon the earlier approaches in two aspects as follows:<sup>15</sup>

- (1) In this study, during the process of segmentation, the fact of mitochondrial double membrane structures is exploited, and the image edges are acquired by explicitly modeling the thick dark membranes, which can have a better performance than the original image edges obtained by the image gradient.
- (2) On the basis of the above-mentioned segmentation results, we utilize the fact that the segmentation results in the continuous layers should maintain consistency, and embed the low-rank property of similar shapes to regularize an active contour model for further optimizing the local misleading segmentation.

The remainder of this study is outlined as follows: In Sec. 2, some related works regarding mitochondrial segmentation on EM data are introduced, and the merits and demerits of two SEM-based methods are detailed. Section 3 gives an indepth presentation of a specific method for mitochondrial segmentation based on the characteristics of ATUM-SEM data. Then, the experimental results are shown to verify the effectiveness of the proposed method in Sec. 4. Finally, in Sec. 5, this study's conclusions are made, and some future research issues are discussed.

## 2. Related Work

In this section, we first describe some of the classical algorithms pertained to image segmentation in the context of this study's proposed method. Then, previous attempts to segment the mitochondria from EM data are introduced. Finally, we broaden our discussion to the trade-offs of two SEM-based methods and briefly mention the image registration technology that is the basis of using the context information.

### 2.1. State-of-the-art segmentation technique

Image segmentation aiming at partitioning an image into a set of disjoint regions has undergone profound examination in computer vision. To date, there have been plenty of brilliant segmentation algorithms developed to tackle this problem in recent decades, such as watersheds,<sup>16</sup> level set,<sup>17</sup> active contour,<sup>18</sup> region growing,<sup>19</sup> and so on. It is noteworthy to emphasize that EM data, with a variety of sub-cellular structures including vesicles, synapses, and membranes, violates the assumption that strong image gradient always corresponds to significant boundaries, which is different from natural images and brings more challenges for segmentation.<sup>14</sup>

### 2.2. Mitochondrial segmentation on EM data

As previously mentioned in Sec. 1, understanding the processes which regulate mitochondrial shapes and functions is very important. Therefore, in recent years, various attempts have been made to quantify the important properties of mitochondria from EM data. In this study, we take a simple review of some recent research about the mitochondrial segmentation of EM data. Aurelien *et al.* considered an automated graph partitioning scheme which was incorporated with shape features. In their study, they first over-segmented the image stack into supervoxels for the purpose of reducing the computational and memory costs by a simple linear iterative clustering (SLIC), followed by embedding the feature vector consisting of Ray descriptors and intensity histograms into the graph.<sup>14</sup> Due to the fact that the Ray features relied on a good binary edge which could not be easily obtained on noisy EM images, they subsequently improved upon their earlier approaches by exploiting the context-aware features instead of the Ray features.<sup>20</sup> Jorstad *et al.* took advantage of the fact that mitochondria have thick dark membranes, and proposed an

active surface-based method for refining the boundary surfaces of mitochondrial segmentation.<sup>21</sup> A recent approach first utilized a parabolic arc model to extract membrane structures, and then employed the curve energy based on active contour to obtain roughly outlined candidate mitochondrial regions, and finally obtained the mitochondrial segmentation by way of a validation process.<sup>11</sup>

### 2.3. Trade-offs

While preferable results were derived from previous research studies, these results have relied on the isotropous characteristic of the data acquired by using focused ion beam scanning electron microscopes (FIB-SEM, Zeiss NVision40).<sup>14,20,21</sup> It has been determined that the FIB-SEM method of high consumption is only limited to small volumes, and is also destructive to the tissues since the sections are lost as soon as they are removed from the block face. In contrast, the ATUM-SEM method does not suffer the damages, and the preserved sections can be imaged and analyzed many times. Furthermore, the ATUM-SEM method can be applied to large volumes for the large-scale statistics and analysis of mitochondrial shapes. In addition, the image acquisition time can be accelerated since the sections collecting on the tape can be parallel imaged using multiple SEMs. Despite the advantages, some challenges still remain, such as the registration of sequential images, and coarse resolution in z-direction.<sup>13</sup>

In order to break through the registration challenge, Saalfeld *et al.* developed an automated registration method for serial sections,<sup>22</sup> and this has been improved by considering the case of wrinkle.<sup>8</sup> This study adopts the improved registration method and two adjacent pictures after registration depicted in Fig. 2 are randomly chosen as the information sources. The image registration techniques are difficult to describe in

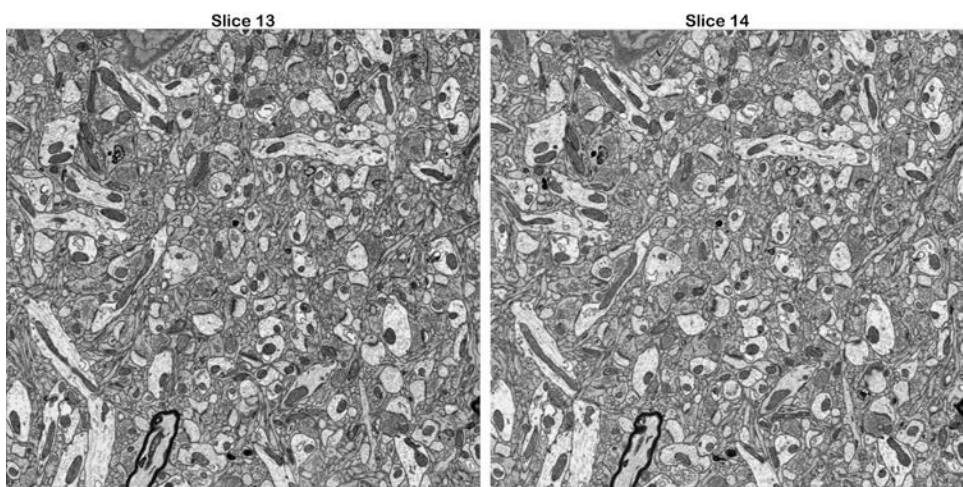


Fig. 2. Two adjacent pictures after image registration.

just a few sentences. Therefore, we refer the interested reader to previous methods for further details regarding the techniques.<sup>8,22</sup>

### 3. Proposed Method

Since the coarse resolution in  $z$ -direction of the ATUM-SEM method limits the use of the previous methods proposed in the isotropic data,<sup>14,20,21</sup> we put forward an automated pipeline for segmenting mitochondria from ATUM-SEM stacks. The proposed algorithm comprises detection, validation for detection, segmentation, and validation for segmentation. The entire flowchart for mitochondrial segmentation is shown in Fig. 3.

#### 3.1. Coarse detection

Adaboost has achieved great success in many applications as a general method for improving the accuracy of any given learning algorithm, especially in regards to image retrieval and face recognition.<sup>23,24</sup> This study recognizes its advantages of fast speed, good performance, and having been implemented in OpenCV. Therefore, the Adaboost algorithm is applied in this study for the detection of the mitochondria. Due to the fact that the machine-learning-based image analysis requires labeled training samples, the following is denoted:  $X_i, i = 1, \dots, 178$  represents the  $i$ th slice and the samples are manually obtained on  $X_1, X_{10}, X_{20}$ , and  $X_{30}$ . The positive samples include the mitochondria and are labeled as +1. Meanwhile, the other are negative samples and labeled as -1. Figure 4 shows some of the specific examples.

Also, in order to obtain a classifier  $\psi$  with better identification ability, these training samples have to fulfill the following criteria:

- The ambiguous samples are required to be removed;
- The proportion of the positive and negative samples are required to be controlled between 1 : 3 and 1 : 5;
- The positive samples are required to be larger than the defined window.<sup>23</sup>

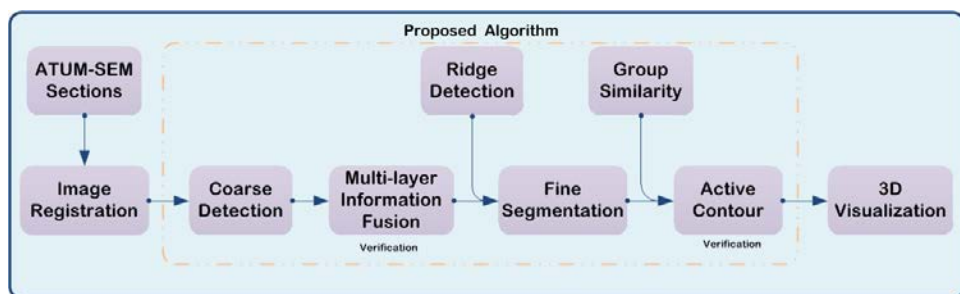


Fig. 3. Complete flowchart for the mitochondrial segmentation.

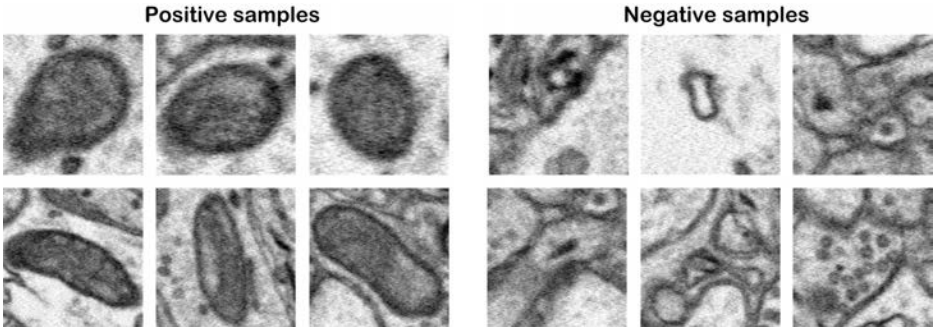


Fig. 4. Some specific examples of the positive and negative samples.

When applying the classifier  $\psi$  to each  $X_i$ ,  $i = 1, \dots, 178$ , each region determined by a sliding window is classified at the multi-scale based on *Haar-like* features.<sup>23</sup> Of course, in more scales the region is classified into positive, the greater possibility the region has to include a mitochondrion. We define  $N_s$  as the number of scales that the region is classified into positive at the multi-scale. Then, the judgements are made as to a given threshold  $\phi$ . The regions with  $N_s$  greater than  $\phi$  are reserved and considered to include the mitochondria. In the experiment, we indicate each region by a red rectangle, which has the same center as the region and has the same size as the largest scales satisfying the region classified into positive. Assume that  $(c_{i,j}^1, c_{i,j}^2)$  and  $(c_{i,j}^3, c_{i,j}^4)$  are, respectively, the top-left and lower-right coordinates of the  $j$ th red rectangle in  $X_i$ . Then we can use  $X_{i,j} = (c_{i,j}^1, c_{i,j}^2, c_{i,j}^3, c_{i,j}^4)$  to solely represent the  $j$ th image domain determined by the  $j$ th red rectangle in  $X_i$ . Some of these results are provided in Sec. 4, and there are found to be mainly three types of identification errors as follows:

- False negatives (the true mitochondria are not identified);
- False positives (the false mitochondria are identified);
- A small number of mitochondria are too long to be totally identified.

Two reasons can account for these errors. The first is that a complex cellular background exists, which contains various types of organelles with different sizes, shapes, texture and brightness. The second is that the pleiomorphic mitochondria appear in many different shapes, based on the cell type and cutting angle. A detailed discussion regarding the most important parameter  $\phi$  has been included in Sec. 4, which represents the minimum detection times at the multi-scale in the Adaboost algorithm.

### 3.2. Multi-layer information fusion

In this section, this study fuses the multi-layer information in order to eliminate the false negatives, and to obtain the mitochondrial connection relationship across the adjacent sections. The main principle can be stated as follows: the mitochondrial sizes are far more than the thickness of the sections. Therefore, a simple conclusion is

drawn, whereby a true mitochondrion  $\mathcal{M}$  is able to exist in the continuous slices. We then define the mitochondrial “length”  $N$  as the number that exists in the continuous slices. A direct solution of eliminating the false negatives is determined to obtain the mitochondrial “length”. Given a mitochondrion  $\mathcal{M}_1$ , the main procedure to judge whether it is true could be summarized as follows:

**Step 1:** Assume that  $X_{i,j}$  is an image domain that the mitochondrion  $\mathcal{M}_1$  first appears in  $X_i$ , and then set the initial slice  $N_0 = i$ . The final slice  $N_1$  in which  $\mathcal{M}_1$  will disappear is unknown and initialized to be 0.

**Step 2:** Denote the central point of  $X_{i,j}$  as  $P_{i,j} = (c_{i,j}^1/2 + c_{i,j}^3/2, c_{i,j}^2/2 + c_{i,j}^4/2)$ , and  $n_i$  as the number of rectangles in the  $i$ th slice. Then we define the distance  $\chi_{i,j}^k$  between  $X_{i,j}$  and  $X_{i+1,k}$  as follows:

$$\chi_{i,j}^k = \|P_{i,j} - P_{i+1,k}\|_2, \quad k = 1, \dots, n_{i+1}. \quad (1)$$

**Step 3:** Assume the maximum offset of a true mitochondrion in adjacent slices to be  $\beta$  pixels. Then, together with the indicative function  $\mathbb{I}$ , the mitochondrial number  $C_{i,j}$  in  $X_{i+1}$  adjacent to  $X_{i,j}$  can be counted as follows:

$$C_{i,j} = \sum_{k=1}^{n_{i+1}} \mathbb{I}\{\chi_{i,j}^k \leq \beta\}. \quad (2)$$

**Step 4:** According to the value  $C_{i,j}$ , the following three cases can be considered here for the sake of narrative clarity as follows:

(C1): In the case of  $C_{i,j} = 0$ , it means that the current layer is a final layer. Set  $N_1 = \max\{N_1, i\}$ ;

(C2): In the case of  $C_{i,j} = 1$ , it means that the current layer is an intermediate layer. There must exist a solely positive integer  $1 \leq k_{i,j} \leq n_{i+1}$  which satisfies the following:

$$k_{i,j} = \arg \min\{\chi_{i,j}^1, \chi_{i,j}^2, \dots, \chi_{i,j}^{n_{i+1}}\}, \quad (3)$$

where  $X_{i+1,k_{i,j}}$  and  $X_{i,j}$  are considered to be connected and represent the same mitochondrion  $\mathcal{M}_1$ . Set  $i = i + 1, j = k_{i,j}$ , and then go back to step 2;

(C3): In the case of  $C_{i,j} = 2$ , it means that the current layer is an intermediate layer and a split has occurred. There exist two positive integers  $1 \leq k_{i,j}^1, k_{i,j}^2 \leq n_{i+1}$  which satisfy the following:

$$k_{i,j}^1 = \arg \min\{\chi_{i,j}^1, \chi_{i,j}^2, \dots, \chi_{i,j}^{n_{i+1}}\}, \quad (4)$$

$$k_{i,j}^2 = \arg \min\{\chi_{i,j}^1, \dots, \chi_{i,j}^{k_{i,j}^1-1}, \chi_{i,j}^{k_{i,j}^1+1}, \dots, \chi_{i,j}^{n_{i+1}}\}, \quad (5)$$

where  $X_{i,j}$  splits into  $X_{i+1,k_{i,j}^1}$  and  $X_{i+1,k_{i,j}^2}$ , which are considered to be connected and represent the same mitochondrion  $\mathcal{M}_1$ . Set  $i = i + 1, j = k_{i,j}^1$ , and  $i = i + 1, j = k_{i,j}^2$ , respectively, and then go back to step 2.

**Step 5:** The “length” of the mitochondrion  $\mathcal{M}_1$  is defined as follows:

$$N = N_1 - N_0 + 1. \quad (6)$$

Of course, a larger “length”  $N$  the mitochondrion  $\mathcal{M}_1$  has, the greater possibility it will have to be true. Then, judgements are made as to a given threshold  $\xi$ , the mitochondrion  $\mathcal{M}_1$  with  $N$  greater than  $\xi$  are considered to be true. The corresponding detection results are reserved to acquire the fine segmentation, and the corresponding connection relationship is reserved to display the 3D Visualization results.

### 3.3. Fine segmentation

In order to obtain a fine segmentation of the mitochondria, this study introduces the following variational image segmentation model<sup>25</sup>:

$$\min_{u \in [0,1]} \left\{ \int_{\mathbf{x} \in X} (g|\nabla u| + fu) d\mathbf{x} \right\}, \quad (7)$$

where  $u$  is a matrix with the same size of image domain  $X$  and can continuously vary between  $[0, 1]$ . The function  $f : X \rightarrow (-\infty, +\infty)$  provides certain hard constraints about the foreground ( $f = -\infty$ ) and background ( $f = \infty$ ) seed regions. In the experiment,  $f$  assigns the central region of  $X$  with a radius of  $\omega$  pixels as  $-9999999$ , the edge of  $X$  as  $9999999$ , and the other region as  $0$ . Define the image edges as  $m$ , the edge detection function  $g \in (0, 1]$  encodes the strong image edges  $m$  as small values, and a common choice for  $g$  is

$$g(m) = \exp(-\alpha|m|^\gamma) \quad (8)$$

with some suitable parameters  $\alpha$  and  $\gamma$ . In previous methods,<sup>15</sup> the image edges were obtained by gradient  $\nabla X$ . Nevertheless, the conventional assumptions that strong image gradient corresponds to significant boundaries does not hold true when confronted with noise and textures inherent in EM data. This results in poor performances for the previous methods on these mitochondria which are in close proximity to vesicles or various membranes.<sup>15</sup> For this reason, we consider enhancing the image edges by utilizing the following ridge detection method.

#### 3.3.1. Ridge detection

Since the bright-dark-bright transition occurs in the membrane profile, the membranes exist at the locations where the intensity increases in opposite directions, and remains stable in the orthogonal directions. Therefore, enhancing the membrane-like structures is an intuitive idea by which to obtain the mitochondrial edges. In order to detect the membranes, we first eliminate the noise in the real images by convolving the image  $X$  with a discrete two-dimensional Gaussian smoothing kernel as follows:

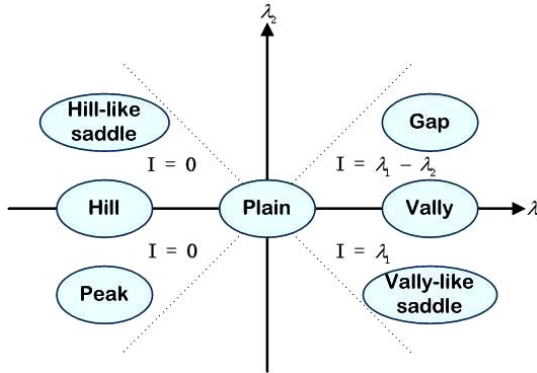


Fig. 5. Topographic shapes to be detected with respect to the eigenvalues of the Hessian matrix, and the assigned ridge energy.

$$G(x, y) = \exp\left(-\frac{x^2 + y^2}{2\delta^2}\right), \quad (9)$$

where the standard deviation  $\delta$  is dependent on the radius  $r$  of the mitochondrial membrane, and a suitable choice is  $\delta = r/\sqrt{3}$ .<sup>26</sup> Then, the second partial derivatives of the image intensity are computed as  $X_{xx}, X_{xy}, X_{yx}, X_{yy}$ , and a Hessian-based ridge detector, which is sensitive to valley-like shapes, is constructed and applied to the image  $X$ . Let  $\lambda_1$  and  $\lambda_2$  be the eigenvalues of Hessian matrix as follows:

$$H = \begin{pmatrix} X_{xx} & X_{xy} \\ X_{yx} & X_{yy} \end{pmatrix}. \quad (10)$$

With no loss of generality, it is assumed that the eigenvalues satisfy  $|\lambda_1| \geq |\lambda_2|$ . As clarified in Fig. 5, a valley is acquired at a location where  $\lambda_1 \gg |\lambda_2|$ . In contrast, the shape seems to be a gap (i.e. a dark blob) when  $\lambda_1 \approx |\lambda_2| \gg 0$ , as shown in the first quadrant of the coordinate system. In the fourth quadrant, a saddle point on a valley is obtained when  $\lambda_1 \gg 0$  and  $\lambda_2 \ll 0$ , which corresponds to a relatively weak point on a membrane. By considering the potential discontinuity in the membranes, the ridge energy is defined as:

$$\mathbf{I} = \mathbb{I}_{\{\lambda_1 > 0\}} \cdot (\lambda_1 - \lambda_2 \cdot \mathbb{I}_{\{\lambda_2 > 0\}}). \quad (11)$$

In the above formulation, the ridge energy in the first quadrant increases while  $\lambda_1$  is increasing, and  $\lambda_2$  is decreasing. In case of the discontinuity of the membrane,  $\lambda_2$  is negative and the energy only depends on the valley depth that is proportional to  $\lambda_1$ . Since the objects which are in the shape of elongated dark stripes, and not hill-like structures (i.e. bright) are favored, the ridge energy in the second and third quadrant is assigned as zero. Then, the ridge energy  $\mathbf{I}$  is normalized to a range of  $[0, 1]$  by using a min-max normalization as follows:

$$\mathbf{I} = \frac{\mathbf{I} - \mathbf{I}_{\min}}{\mathbf{I}_{\max} - \mathbf{I}_{\min}}, \quad (12)$$

where  $\mathbf{I}_{\max}$  and  $\mathbf{I}_{\min}$  correspond to the maximum and minimum intensity in ridge energy  $\mathbf{I}$ , respectively. In this study, the minimization is achieved by the following energy function:

$$\min_{u \in [0,1]} \left\{ \int_{\mathbf{x} \in X} (g(\mathbf{I})|\nabla u| + fu) d\mathbf{x} \right\}. \quad (13)$$

### 3.3.2. Computing the solution

To minimize model (13), an equivalent model with an auxiliary variable  $v$  is proposed<sup>27</sup>:

$$\min_{u,v} \left\{ \int_{\mathbf{x} \in X} g(\mathbf{I})|\nabla u| + \frac{\theta}{2}(u-v)^2 + fv d\mathbf{x} \right\}. \quad (14)$$

It should be noted that model (14) could approximate model (13) when  $\theta \rightarrow \infty$ , and it is an optimization problem about two variables,  $u$  and  $v$ , which can be solved by alternatively optimizing:

$$u^{n+1} = \arg \min_u \left\{ \int_{\mathbf{x} \in X} g(\mathbf{I})|\nabla u| + \frac{\theta}{2}(u-v^n)^2 d\mathbf{x} \right\} \quad (15)$$

and

$$v^{n+1} = \arg \min_v \left\{ \int_{\mathbf{x} \in X} \frac{\theta}{2}(u^{n+1}-v)^2 + fv d\mathbf{x} \right\}. \quad (16)$$

Note that the sub-optimization problem (15) exactly resembles the Total Variation denoising model (ROF) presented by Rudin, Osher and Fatemi,<sup>28</sup> where  $\theta$  is now a spatial regularization parameter. The outline of the alternating minimization procedure is as follows:

**Step 1:** Solution for  $u^{n+1}$  with a fixed  $v^n$ .

The only difference found between (15) and the original ROF model is in the g-weighting of the Total Variation norm, which does not produce any additional difficulty for the solution. In order to solve this sub-optimization problem, the following adapted version of the projected gradient descend algorithm is used<sup>29</sup>:

$$\begin{aligned} \hat{\mathbf{t}}^{n+1} &= \mathbf{t}^n + \theta \cdot \tau \nabla u^n \\ \mathbf{t}^{n+1} &= \frac{g(\mathbf{I})\hat{\mathbf{t}}^{n+1}}{\max\{g(\mathbf{I}), |\hat{\mathbf{t}}^{n+1}|\}} \\ u^{n+1} &= v^n + \frac{\nabla \cdot \mathbf{t}^{n+1}}{\theta}. \end{aligned} \quad (17)$$

where  $\mathbf{t}$  is the dual variable; and time step  $\tau$  is used to guarantee the scheme to remain stable. It has also been pointed out that  $\tau \leq 1/2d$  holds true for the  $d$ -dimensional problems.<sup>29</sup>

**Step 2:** Solution for  $v^{n+1}$  with a fixed  $u^{n+1}$ .

Note that (16) is an element-wise optimization problem, which is easy to solve. The Euler–Lagrange equation for (16) is given by

$$\theta(v^{n+1} - u^{n+1}) + f = 0. \quad (18)$$

Where the following is acquired:

$$v^{n+1} = (u^{n+1}\theta - f)/\theta. \quad (19)$$

**Step 3:** Repeat step 1 and step 2 until convergence is achieved.

In this study's experiment,  $u$  is first initialized at 0.5. Following alternative iteration until convergence, a binary image is obtained by thresholding at 0.5. The white region  $u > 0.5$  is considered as the segmentation result of the mitochondrion. This model is applied to every reserved detection result after multi-layer information fusion. we can obtain the desirable segmentation results, some of which are presented in Sec. 4.

### 3.4. Verification by context

In this section, we focus on utilizing the context information to rectify the local misleading segmentation. Assume that the “length” of mitochondrion  $\mathcal{M}$  is  $n$ . By utilizing the connection relationship and above segmentation results, a sequence of consecutive binary images  $\{M_1, \dots, M_n\}$  for  $\mathcal{M}$  are obtained. Then, we try to find a set of contours  $\{\mathcal{C}_1, \dots, \mathcal{C}_n\}$  to optimize the segmentation results from the binary images. In order to keep the contours similar to each other, the following model with the low-rank property of similar shapes embedded is used<sup>30</sup>:

$$\min_{\mathbf{X}} \sum_{i=1}^n f_i(\mathcal{C}_i) + \lambda \|\mathbf{X}\|_{*}. \quad (20)$$

Here  $\|\mathbf{X}\|_{*}$  is the nuclear norm of  $\mathbf{X} = [\mathcal{C}_1, \dots, \mathcal{C}_n]$ , and  $f_i(\mathcal{C}_i)$  is the energy functional of the region-based active contour model:

$$f_i(\mathcal{C}_i) = \int_{\Omega_1} (M_i(x) - u_1)^2 dx + \int_{\Omega_2} (M_i(x) - u_2)^2 dx + \eta \text{ length } (\mathcal{C}_i), \quad (21)$$

where  $\Omega_1$  and  $\Omega_2$  represent the regions inside and outside the contour, respectively; and  $u_1$  and  $u_2$  denote the mean intensity of  $\Omega_1$  and  $\Omega_2$ , respectively. Then, in order to optimize the objective energy function, a Proximal Gradient method and singular value thresholding algorithm are used.

The concrete details for solving the model (20) can be found,<sup>30</sup> and only the iterative procedure is provided as follows:

$$\mathbf{X}^{k+1} = \mathcal{D}_{\frac{\lambda}{\mu}} \left( \mathbf{X}^k - \frac{1}{\mu} \nabla F(\mathbf{X}^k) \right), \quad (22)$$

where  $k$  is the iterative time,  $\nabla F(\mathbf{X}^k) = [\nabla f_1(\mathcal{C}_1^k), \dots, \nabla f_n(\mathcal{C}_n^k)]$ , and  $\mathcal{D}_{\frac{\lambda}{\mu}}$  with

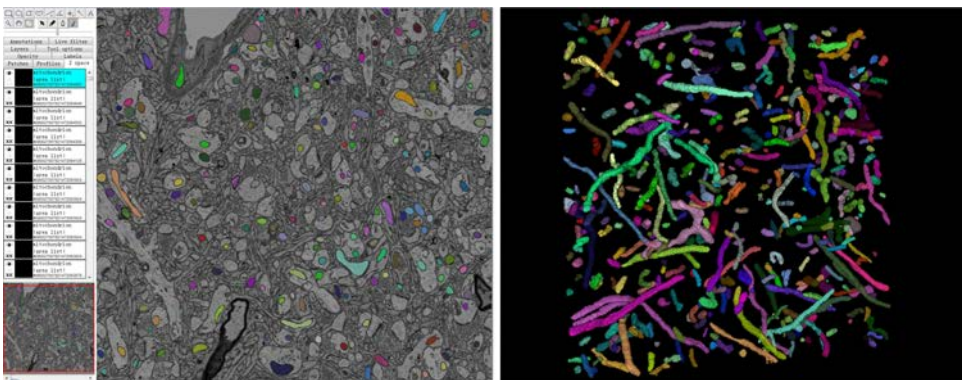


Fig. 6. Left: Ground truth data via hand segmentation in the ImageJ software; Right: 3D visualization exhibition of the ground truth in the first 30 slices.

constant  $\mu$  controlling the step-length of the curve evolution in each iteration is a singular value thresholding operator.

## 4. Experimental Results

We first provide some details related to the ground truth data and the corresponding experimental results of proposed method. Then, some relevant experiments are broadened and some useful discussions are provided.

### 4.1. *Ground truth*

The ground truth data were prepared via the hand segmentation outlining the inner membrane of a total of 434 mitochondria which had appeared in the first 30 slices using the ImageJ software. The left picture in Fig. 6 depicts the ground truth in one slice where different colors represent different mitochondria. The right picture exhibits the 3D visualization results obtained by the ImageJ software.<sup>31</sup> It should be emphasized that generating such a ground truth database required a considerable amount of human effort, and it was also a very time consuming process, which served to justify that computerized segmentation is liable to accelerate tomographic analyses.

### 4.2. *Results of proposed method*

In this section, we detailedly present the results of proposed method including the mitochondrial detection results, segmentation results, and 3D visualization results.

#### 4.2.1. *Detection results*

In Fig. 7 of this section, some of the detection results are presented. The left picture shows some detected mitochondria which are indicated by the red rectangles via an

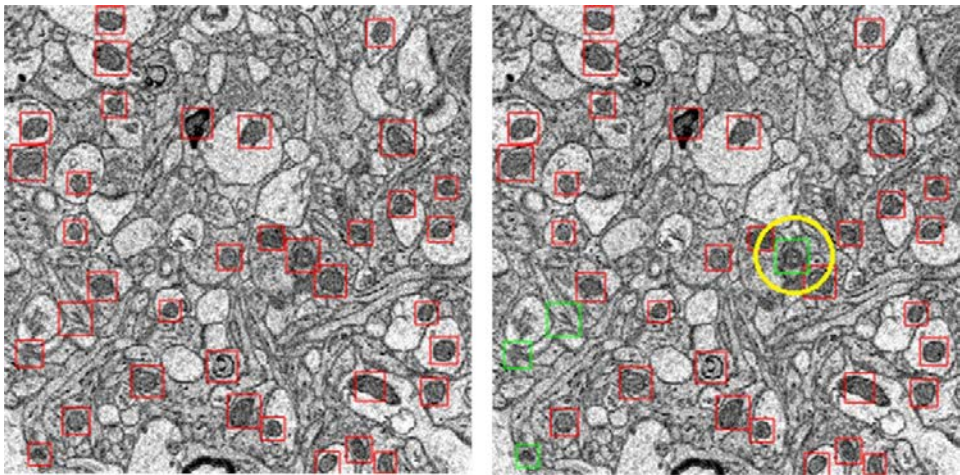


Fig. 7. Left: Detection results of the Adaboost algorithm; Right: Red rectangles are reserved and the green rectangles are deleted after the multi-layer information fusion, and one green rectangle indicated by the yellow circle is mistakenly deleted.

Adaboost algorithm. In the right picture, the mitochondria represented by the red rectangles appear more than  $\xi$  continuous slices and are considered as true. Meanwhile, the mitochondria represented by the green rectangles are considered as false after the multi-layer information fusion. Since the detection results acting as a crucial role in the experimental results are the basis of the segmentation, at this point a discussion regarding the adjustment of the two important parameters  $\phi$  in the Adaboost algorithm, and  $\xi$  in multi-layer information fusion is conducted. In this study, the detection accuracy is measured by the two fundamental performance indicators, *precision* and *recall*. The *precision* is computed as the ratio of the detection outcome being correct, and the *recall* provides the ratio of the true elements being successfully detected, i.e.

$$\text{precision} = \text{True Pos}/(\text{True Pos} + \text{False Pos}), \quad (23)$$

$$\text{recall} = \text{True Pos}/(\text{True Pos} + \text{False Neg}). \quad (24)$$

Then, inspired by the preceding definition,<sup>32</sup> this study defines that a detection result is considered as positive if the area of overlap between the detection region and corresponding ground truth occupies at least 70% of the area of the ground truth. Then, the *precision* and *recall* are defined on the number of regions, rather than the sizes of regions. Such a definition ensures an accuracy measurement which satisfies

Table 1. Average *precision* and *recall* graph versus the validity threshold  $\phi$ .

$\phi$	1	2	3	4	5	6	7	8	9	10	11	12	13	14	15
<i>precision</i>	0.868	0.883	0.882	0.881	0.877	0.870	0.863	0.856	0.845	0.836	0.829	0.821	0.813	0.804	0.797
<i>recall</i>	0.148	0.212	0.276	0.333	0.381	0.427	0.469	0.506	0.535	0.565	0.590	0.614	0.634	0.651	0.668

Table 2. Average *precision* and *recall* graph versus the validity threshold  $\xi$ , respectively, at validity threshold  $\phi = 4, 5$ , and  $6$ .

$\xi$	0	1	2	3	4	5	6	7	8	9	10
<i>precision</i>	$\phi = 4$	0.881	0.860	0.828	<b>0.782</b>	0.706	0.623	0.569	0.506	0.445	0.403
	$\phi = 5$	0.877	0.855	0.821	0.773	0.695	0.611	0.559	0.494	0.443	0.400
	$\phi = 6$	0.869	0.846	0.809	0.759	0.685	0.598	0.547	0.487	0.438	0.398
<i>recall</i>	$\phi = 4$	0.333	0.497	0.614	<b>0.712</b>	0.774	0.831	0.862	0.887	0.897	0.918
	$\phi = 5$	0.381	0.545	0.656	0.744	0.806	0.851	0.878	0.903	0.914	0.928
	$\phi = 6$	0.427	0.589	0.697	0.773	0.830	0.871	0.898	0.914	0.923	0.928

that each region is evaluated, depending on whether or not it contains a single mitochondrion. Together with the ground truth, the *precision* and *recall* of the detection results in each slice could then be computed.

We provide the average *precision* and *recall* graph versus the validity threshold  $\phi$  ranging from 1 to 15 in Table 1. It can be seen that the *precision* increases with the increase of  $\phi$  while the *recall* has a maximum at  $\phi = 2$ . Since the *precision* can be improved by fusing the multi-layer information, we are here prone to choose a smaller validity threshold  $\phi$ , which can ensure a higher *recall* and allow a lower *precision*. Some experiments are conducted for comparison at  $\phi = 4, 5$ , and  $6$ . Table 2, respectively, provides the average *precision* and *recall* graph versus the validity threshold  $\xi$ . In this paper, the validity threshold  $\phi$  and validity threshold  $\xi$  are, respectively, chosen as 4 and 3, the corresponding *precision* and *recall* are 0.782 and 0.712, which are marked in bold for distinction in Table 2. Some alternative selection method can be  $\phi = 5, \xi = 3$  and  $\phi = 6, \xi = 2$ . In general, each selection method has its own emphasis and they can achieve the similar performance. Since the focus in this paper is on the segmentation of mitochondria, we do not have more discussion on which selection method is optimal. The left picture in Fig. 8 demonstrates the average *precision* and *recall* graph in the first 30 slices with respect to the

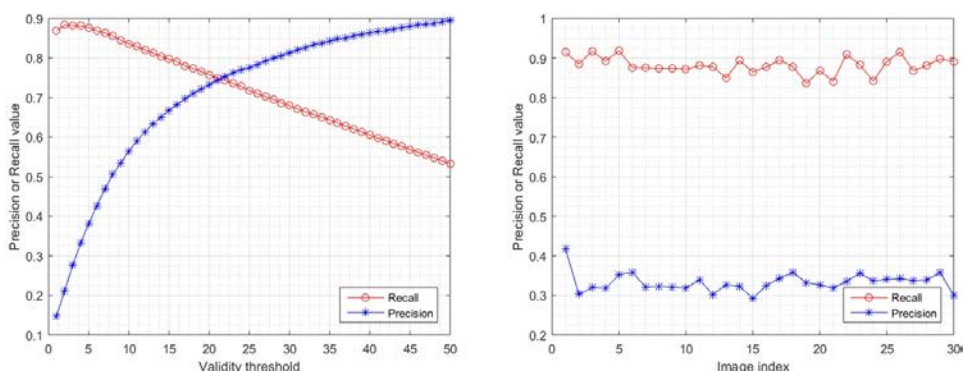


Fig. 8. Left: Average *precision* and *recall* graph in the first 30 slices versus the validity threshold  $\phi$ ; Right: Respective *precision* and *recall* of each slice at  $\phi = 4$ .

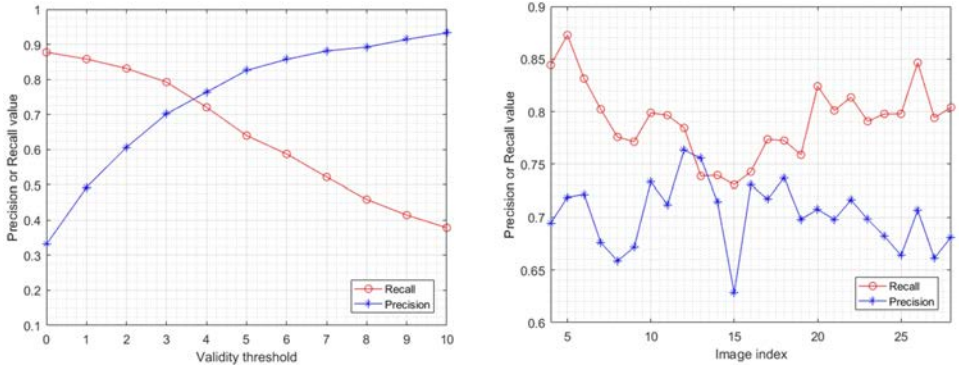


Fig. 9. Left: *Precision* and *recall* graph from slices 4–28 versus the validity threshold  $\xi$ ; Right: Respective *precision* and *recall* from slices 4–28 at  $\xi = 3$ .

Table 3. List of the parameters and settings used in the implementation.

Parameters	$\phi$	$\beta$	$\xi$	$\alpha$	$\gamma$	$\omega$	$r$	$\delta$	$\theta$	$\tau$	$\lambda$	$\eta$	$\mu$
Settings	4	50	3	10	0.55	15	9	$9/\sqrt{3}$	10	0.245	1	1	1

validity threshold  $\phi$ , ranging from 1 to 50. Specifically, the respective *precision* and *recall* value in each slice is shown in the right picture in Fig. 8 at validity threshold  $\phi = 4$ . On this basis, we fuse the multi-layer information to eliminate the false negatives. For fairness purposes, we only compute the *precision* and *recall* of the detection results in slices 4–28, since a small number of mitochondria may have disappeared in the initial slices, or emerged in the terminative slices. The left picture in Fig. 9 demonstrates the average *precision* and *recall* graph in slices 4–28 for the reserved detection results, with respect to the validity threshold  $\xi$ , ranging from 0 to 10. Analogously, the respective *precision* and *recall* value in slices 4–28 is shown in the right picture in Fig. 9 at validity threshold  $\xi = 3$ . The aforementioned parameters and settings used in the system are presented in Table 3.

#### 4.2.2. Segmentation results

In this section, we first provide the specific segmentation results of one mitochondrion existing in slices 1–9 in Fig. 10. Wherein, from the top to the bottom, each row represents the detected results, corresponding ground truth, segmentation results by previous methods, segmentation results after enhancing the image edges, and segmentation results after verification by context, respectively. It can be seen that the segmentation results after enhancing the image edges (in the fourth line) have obviously better performance abilities than the results obtained by previous methods (in the third line). This is particularly evident against these mitochondria adjacent to vesicles or various membranes, such as in slices 1–3. Moreover, the final segmentation

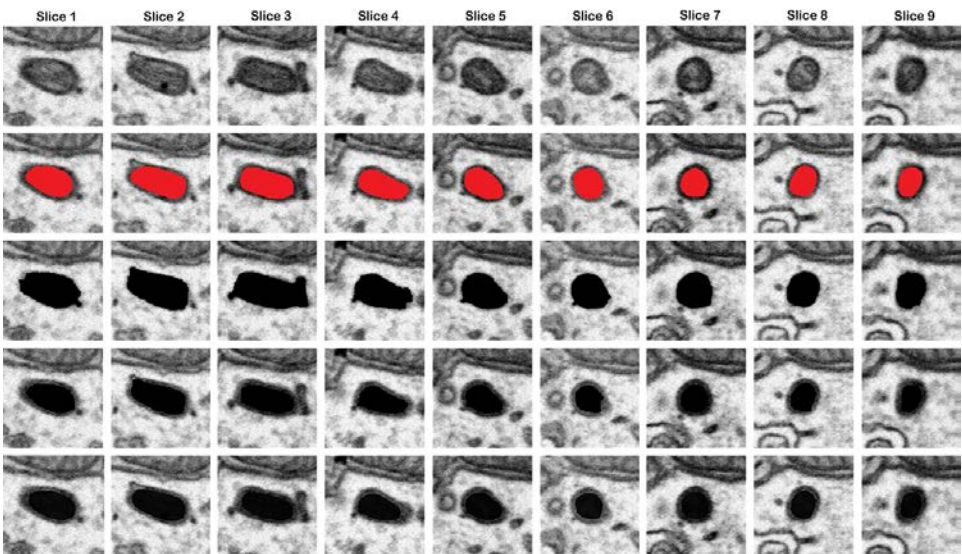


Fig. 10. One specific example of the mitochondrion existing in slices 1–9. From top to bottom: each row represents the detection results, corresponding ground truth, segmentation results by previous methods, segmentation results after enhancing the image edges, and segmentation results after verification by context, respectively.

results (bottom row) take advantage of the shape information in context, which further increases the robustness and smoothness. As shown in slices 2 and 6, the verification by context rectifies the local misleading segmentation results and makes the segmentation similar, which is the way mitochondria should be in continuous slices.

For the quantitative results, we use the ground truth data to evaluate the segmentation results on each of the reserved detection results according to the so-called *Jaccard index*, or the *VOC score* to measure the segmentation quality.<sup>14</sup> *RG* and *VbC* denote the segmentation results in the previous methods,<sup>15</sup> and the segmentation results after verification by context in this study, respectively. For these two types of segmentation results, we compute their corresponding *VOC score* as follows:

$$\text{VOC score} = \text{True Pos}/(\text{True Pos} + \text{False Pos} + \text{False Neg}), \quad (25)$$

which is the ratio of the areas of the intersection between the segmentation result and the ground truth, and of their union. The *VOC score* of one slice is defined as the average *VOC score* of each detected result and the *VOC error* is defined as  $1 - \text{VOC score}$ . Additionally, this study also considers using the *Rand error* similarly defined as  $1 - \text{Rand index}$ , where *Rand index* measures the accuracy with which pixels are associated to their respective regions.<sup>33</sup> The *VOC error* and the *Rand error* between the two types of segmentation results, along with the ground truth in each slice, are displayed in Fig. 11. It can be seen that the final segmentation

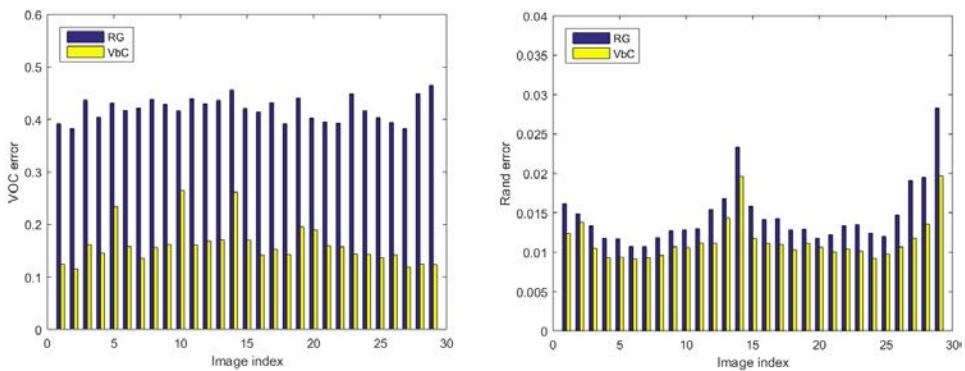


Fig. 11. Average *VOC error* and *Rand error* between the two types of segmentation results and the ground truth in each slice.

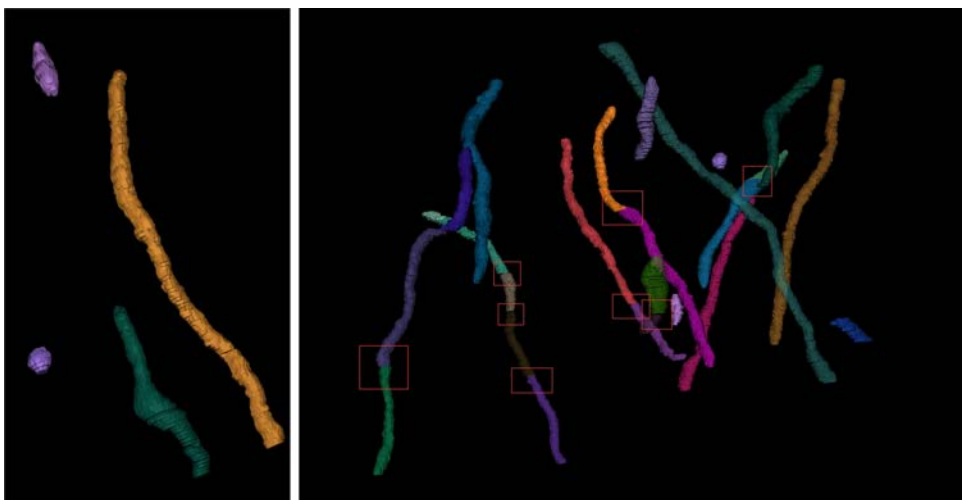


Fig. 12. Computerized segmentation results. Left: Four whole mitochondria in different shapes; Right: 3D visualization exhibition of the partial mitochondria.

results display consistently smaller errors, regardless of the *VOC error* and *rand error*, when compared to the previous results in each slice,<sup>15</sup> and closely match the performances of the human annotators in this study.

#### 4.2.3. 3D visualization

The segmentation results after verification by context are subsequently imported into the ImageJ software and the computerized segmentation results are obtained, as shown in Fig. 12. The left picture reveals the 3D visualization results of the four whole mitochondria, from which it can be seen that there are evident variations in the mitochondrial sizes. The smallest mitochondrion resembles an ellipsoid with a

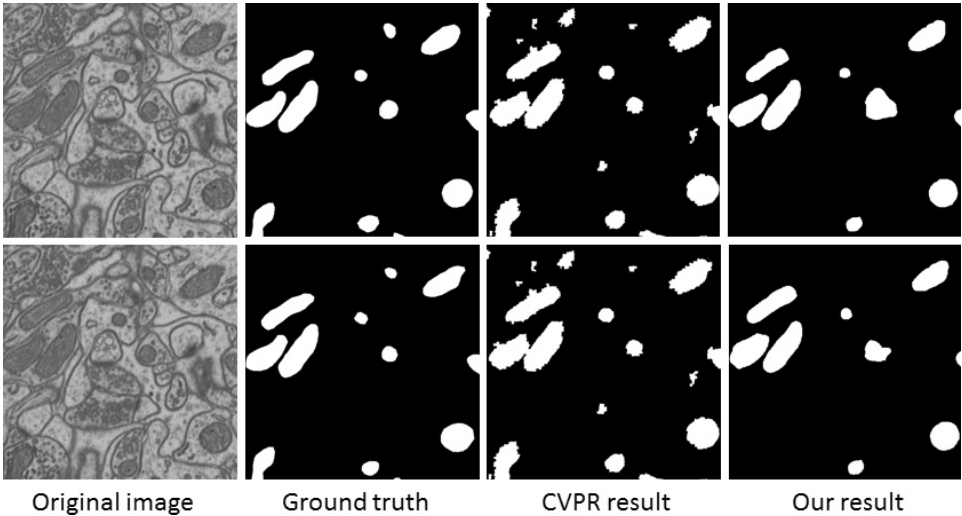


Fig. 13. From left to right: original image, ground truth, CVPR result and proposed segmentation result.

diameter of approximately  $0.4 \mu\text{m}$  since it exists in eight slices. In contrast, the largest mitochondrion is found to be tubular, with a length of approximately  $6 \mu\text{m}$ . The right picture in Fig. 12 also shows the 3D visualization results of the partial mitochondria with the split errors indicated by the red rectangles, although they can be easily solved by a merge operation in the ImageJ software.

#### 4.3. Discussion

In this section, we broaden our experiments on proposed segmentation method on an available benchmarks (FIB-SEM data) and recent deep learning methods on annotated ATUM-SEM data, and provide some useful discussions on the experimental results.

##### 4.3.1. Proposed segmentation method on FIB-SEM data

In this section, we explore whether the proposed method has the general applicability to an available benchmark (FIB-SEM data). The dataset including training data and testing data is downloaded from the webpage<sup>a</sup> and the resolution of each voxel is approximately  $5 \times 5 \times 5 \text{ nm}$ . The segmentation results of the testing data were produced with the algorithm presented in the CVPR13 publication.<sup>34</sup> When applying the proposed method, we have attempted to train the Adaboost classifier  $\psi$  with the training data. Unfortunately, the classifier  $\psi$  does not produce satisfying detection results on FIB-SEM data as it does on ATUM-SEM data. It may be caused by many reasons, such as the higher resolution (2 nm in plane) of ATUM-SEM data, and the obvious differences can be seen from Fig. 13 (Left: original FIB-SEM image)

<sup>a</sup><http://cvlab.epfl.ch/data/em>.

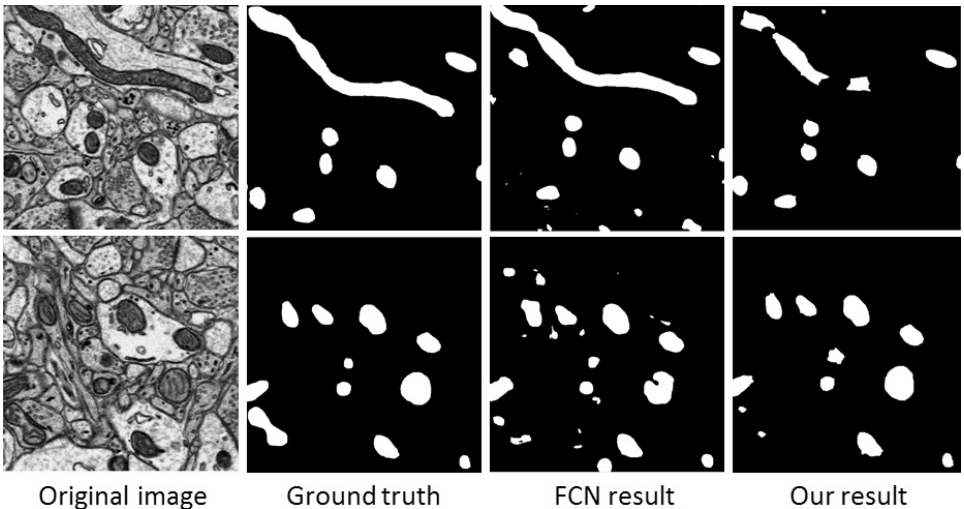


Fig. 14. From left to right: original image, ground truth, FCN result and proposed segmentation result.

and Fig. 14 (Left: original ATUM-SEM image). Since the main contributions in the manuscript consist in the process of segmentation, namely, obtaining the image edges of variational model by ridge detection rather than by image gradient, and utilizing the group-similarity in context to optimize the local misleading segmentation, we test the proposed segmentation method by several given detection results. According to size of mitochondrial membrane, we adjust the parameters: radius  $r = 4$  and standard deviation  $\delta = 4/\sqrt{3}$  in the experiment. After segmentation, we choose the segmentation result on slice 1 (top) and slice 2 (down) and provide the original image, ground truth, CVPR result<sup>34</sup> and our result from left to right in Fig. 13. We can see that our segmentation results are indeed smoother than CVPR segmentation results, and closely match the ground truth. Nevertheless, it should be pointed out when the mitochondrial membrane is blurry and the image edge of variational model is hard to obtain, the segmentation will overflow and segmentation error will emerge.

#### 4.3.2. Fully convolutional network on ATUM-SEM data

In this section, we compare the proposed method with the frequently-used convolutional neural networks (CNN) on produced dataset. In the experiment, we first divide the annotated dataset into training data and testing data. Then we use the VGG16's first 4 blocks to get CNN features,<sup>35</sup> and combine upsampling and skip layers to construct the fully convolutional neural networks (FCN).<sup>36</sup> After that we train the FCN end-2-end on the segmentation training data. The architect of FCN based on VGG16 is presented in Table 4. We apply the network to the testing data which ranges from slice 21 to 30, and then compute the average *VOC error* and *rand*

Table 4. The architect of FCN based on VGG16.

Layer	Operation	Kernel	Output channel
VGG16 4th block last conv feature map			512
Up4	Upsampling	$2 \times 2$	512
Conv5	Concatenate VGG16 3rd block conv feature map and up4		768
Conv5_1	Conv/Relu	$1 \times 1$	256
Conv5_2	Conv/Relu	$3 \times 3$	256
Conv5_3	Conv/Relu	$3 \times 3$	256
Up5	Upsampling	$2 \times 2$	256
Conv6	Concatenate VGG16 2nd block conv feature map and up5		384
Conv6_1	Conv/Relu	$1 \times 1$	128
Conv6_2	Conv/Relu	$3 \times 3$	128
Conv6_3	Conv/Relu	$3 \times 3$	128
Up6	Upsampling	$2 \times 2$	128
Conv7	Concatenate VGG16 2nd block conv feature map and up6		192
Conv7_1	Conv	$1 \times 1$	64
Conv7_2	Conv	$3 \times 3$	64
Conv7_3	Conv	$3 \times 3$	64
Conv8	Conv	$1 \times 1$	32
Conv8_1	Conv	$3 \times 3$	32
Conv8_2	Conv	$3 \times 3$	32
Softmax	Softmax		2

Table 5. Average *VOC error* and *rand error* in each slice.

Slice	21	22	23	24	25	26	27	28	29	30
<i>VOC error</i>	0.333	0.315	0.301	0.345	0.303	0.318	0.296	0.298	0.336	0.350
<i>rand error</i>	0.015	0.015	0.012	0.016	0.014	0.016	0.019	0.019	0.014	0.013

*error* between the segmentation results and the ground truth in each slice. The corresponding errors are displayed in Table 5.

To have a visual understanding, we choose partial segmentation result from slice 29 and provide the original image, ground truth, FCN result and our result from left to right in Fig. 14. We can see that proposed segmentation method performs preferable results on regular mitochondria but not on elongated mitochondria. Meanwhile, the FCN based on VGG16 has a good performance on those mitochondria with elongated shapes, but it is easy to confuse the mitochondria with other sub-cellular structures, namely producing additional segmentation results of sub-cellular structures. Although some post-processing technology will improve the segmentation performance of FCN, such as deleting the regions with small area and grotesque

shape, it would be more interesting if the two segmentation results can be combined. Future research in this area will investigate the two methods.

## 5. Conclusion

In this research study, in order to investigate the link between the mitochondrial physical structures and the corresponding functions, an ATUM-SEM method provides sufficient resolution to look into the details, and also produces substantial amounts of data. Consequently, we have proposed a coarse-to-fine method for mitochondrial segmentation and showed the 3D visualization results in the ImageJ software. It should be noted that the proposed method is completely automated, with the exception of manual labels for training the Adaboost classifier  $\psi$  and the final manual validation process. All of these were operated in the ImageJ software, not consuming many human work hours.

When compared to the previous methods proposed on the isotropous FIB-SEM data, this study's method can be generalized to a more widely applicable EM data, which allows a coarse resolution in the  $z$ -direction. Moreover, this study proposes to acquire the membrane edges by using ridge detection instead of image gradient, and then uses the context for verification, and finally overcomes the previous limitations on these mitochondria near the vesicles or various membranes. It should be noted that, although the obtained mitochondria are just some initial results, the significance is found to be remarkable.

Despite the preferable segmentation results of this study's approach, there are still many problems needed to be solved along the line of the present research. These problems include the detection process and the multi-layer information fusion process. One reason is that some of the mitochondria parallel to the slice direction display extremely elongated shapes, they are difficult to be totally detected. What is worse, a minority of the mitochondria do not present the mitochondrial structure characteristics, and they are difficult to be identified in one slice, even manually. Therefore, it is natural to explore the use of other algorithms, or consider embedding the multi-layer information into the detection algorithms. Beside, a better connection relationship should be obtained, such as using the segmentation information, to reduce the split errors, as pointed out in Fig. 12. Inspired from Chen *et al.*,<sup>37</sup> it may be a better idea to go beyond the traditional coarse-to-fine method (segmentation after detection) and segment the mitochondria directly from the EM data by the deep learning method. In the future, we will attempt to quantitatively analyse and compare the two kind of methods, a coarse-to-fine method and a direct segmentation method. Future research in this area will investigate the two methods, and will focus on optimizing the segmentation results.

## Acknowledgments

The authors would like to thank reviewers for their valuable comments and suggestions that helped improve the original version of this paper, thank Dr. Yu Kong, Yang Yang and Danqian Liu (Institute of Neuroscience, CAS) for their assistance with preparation and sectioning of the sample. Also, we would like to thank Mr. Lixin Wei and his colleagues (Institute of Automation, CAS) for the Zeiss Supra55 SEM and technical support. This research study is supported by the Special Program of Beijing Municipal Science & Technology Commission (No. Z161100000216146), Strategic Priority Research Program of the CAS (No. XDB02060001), National Science Foundation of China (No. 61673381, No. 61201050, No. 61306070) and the Institute of Automation, CAS, for the 3D Reconstruction of Brain Tissue at Synaptic Level (No. Y3J2031DZ1).

## References

1. Anesti V, Scorrano L, The relationship between mitochondrial shape and function and the cytoskeleton, *BBA-Gen Subjects* **1757**:692–699, 2006.
2. Mumcuoglu EU *et al.*, Computerized detection and segmentation of mitochondria on electron microscope images, *J Microsc* **246**:248–265, 2012.
3. Campello S, Scorrano L, Mitochondrial shape changes: Orchestrating cell pathophysiology, *EMBO Rep* **11**:678–684, 2010.
4. Kroemer G, Mitochondria in cancer, *Oncogene* **25**:4630–4632, 2006.
5. Gogvadze V, Orrenius S, Zhivotovsky B, Mitochondria in cancer cells: What is so special about them? *Trends Cell Bio* **18**:165–173, 2008.
6. Wallace DC, Mitochondria and cancer, *Nat Rev Cancer* **12**:685–698, 2012.
7. Simone F, Lorenzo G, Guido K, Targeting mitochondria for cancer therapy, *Nat Rev Drug Discov* **9**:447–464, 2010.
8. Chen X, Xie QW, Shen LJ, Han H, Wrinkle image registration for serial microscopy sections, *IEEE Computer Society 2015 11th Int Conf Signal-Image Technology Internet-Based Systems*, pp. 23–26, 2015.
9. Liu T, Jones C, Seyedhosseini M, Tasdizen T, A modular hierarchical approach to 3D electron microscopy image segmentation, *J Neurosci Meth* **226**:88–102, 2014.
10. Narayanan K *et al.*, Saturated reconstruction of a volume of neocortex, *Cell* **162**:648–661, 2015.
11. Tasel SF, Mumcuoglu EU, Hassanpour RZ, Perkins G, A validated active contour method driven by parabolic arc model for detection and segmentation of mitochondria, *J Struct Biol* **194**:253–271, 2016.
12. Mannella C, Marko M, Buttle K, Reconsidering mitochondrial structure: New views of an old organelle, *Trends Biochem Sci* **22**:37–38, 1997.
13. Briggman KL, Bock DD, Volume electron microscopy for neuronal circuit reconstruction, *Curr Opin Neurobiol* **22**:154–161, 2012.
14. Aurelien L, Smith K, Achanta R, Knott G, Fua P, Supervoxel-based segmentation of mitochondria in EM image stacks with learned shape features, *IEEE Trans Med Imaging* **31**:474–486, 2011.
15. Li WF *et al.*, Segmentation of mitochondria based on SEM images, *IEEE Conf. Mechatronics and Automation*, pp. 1953–1959, 2016.
16. Vincent L, Soille P, Watersheds in digital spaces: An efficient algorithm based on immersion simulations, *IEEE T Pattern Anal* **13**:583–598, 1991.

W. Li et al.

17. Sethian JA, A fast marching level set method for monotonically advancing fronts, *P Natl Acad Sci USA* **93**:1591–1595, 1996.
18. Kass M, Witkin A, Terzopoulos D, Snakes: Active contour models, *Int J Comput Vision* **1**:321–331, 1988.
19. Zhu SC, Yuille A, Region competition: Unifying snakes, region growing, and Bayes/MDL for multi-band image segmentation, *IEEE T Pattern Anal* **18**:884–900, 1996.
20. Aurelien L, Becker C, Neila PM, Fua P, Exploiting enclosing membranes and contextual cues for mitochondria segmentation, *Medical Image Computing and Computer-Assisted Intervention*, pp. 65–72, 2014.
21. Jorstad A, Fua P, Refining mitochondria segmentation in electron microscopy imagery with active surfaces, *Computer Vision-ECCV*, pp. 325–329, 2014.
22. Saalfeld S, Cardona A, Hartenstein V, Tomancak P, As-rigid-as-possible mosaicking and serial section registration of large ssTEM datasets, *Bioinformatics* **26**:57–63, 2010.
23. Viola P, Jones MJ, Robust real-time face detection, *Int J Comput Vision* **57**:137–154, 2004.
24. Pavani SK, Delgado D, Frangi AF, Haar-like features with optimally weighted rectangles for rapid object detection, *Pattern Recogn* **43**:160–172, 2010.
25. Roberts M et al., Neural process reconstruction from sparse user scribbles, *Medical Image Computing and Computer-Assisted Intervention*, pp. 621–628, 2011.
26. Steger C, An unbiased detector of curvilinear structures, *IEEE T Pattern Anal* **20**:113–125, 1998.
27. Unger M, Pock T, Bischof H, Continuous globally optimal image segmentation with local constraints, *Computer Vision Winter Workshop*, 2008.
28. Rudin LI, Osher S, Fatemi E, Nonlinear total variation based noise removal algorithms, *Physica D* **60**:259–268, 1992.
29. Chambolle A, Total variation minimization and a class of binary MRF models, *5th Int Workshop Energy Minimization Methods in Computer Vision and Pattern Recognition*, pp. 136–152, 2005.
30. Zhou XW, Huang XJ, Duncan JS, Yu WC, Active contours with group similarity, *IEEE Conf Computer Vision and Pattern Recognition*, pp. 2969–2976, 2013.
31. Schmid B, Schindelin J, Cardona A, Longair M, Heisenberg M, A high-level 3D visualization api for Java and ImageJ, *BMC Bioinformatics* **11**:1–7, 2010.
32. Tasel SF, Hassanpour R, Mumcuoglu EU, Automatic detection of mitochondria from electron microscope tomography images: A curve fitting approach, *SPIE Medical Imaging, International Society for Optics and Photonics*, pp. 1314–1314, 2014.
33. Rand WM, Objective criteria for the evaluation of clustering methods, *J Am Stat Assoc* **66**:846–850, 1971.
34. Aurelien L, Li Y, Fua P. Learning for structured prediction using approximate subgradient descent with working sets, *IEEE Conf Computer Vision and Pattern Recognition*, pp. 1987–1994, 2013.
35. Simonyan K, Zisserman A, Very deep convolutional networks for large-scale image recognition, arXiv preprint, *arXiv:1409.1556*, 2014.
36. Long J, Shelhamer E, Darrell T, Fully convolutional networks for semantic segmentation, *IEEE Conf Computer Vision and Pattern Recognition*, pp. 3431–3440, 2015.
37. Chen J et al., Combining fully convolutional and recurrent neural networks for 3D biomedical image segmentation, *29th Conf Neural Information Processing Systems*, pp. 3036–3044, 2016.



**Weifu Li** received his B.S. degree in Applied Mathematics from Hubei University, China, in 2014. He is currently a M.S. candidate in Faculty of Applied Mathematics, Hubei University. His current research interests include image processing, computational neuroscience and deep learning.



**Hao Deng** received his M.S. degree in Applied Mathematics from Hubei University, China, in 2016. He is currently a Ph.D. candidate in Faculty of Information Technology, Macau University of Science and Technology, Macau, China. His current research interests include image processing, neural network and pattern recognition.



**Qiang Rao** received his B.S. degree in Automation Engineering from Xi'an Jiaotong University, China, in 2014. He is currently a M.S. candidate in Pattern Recognition and Artificial Intelligence in Chinese Academy of Sciences Institute of Automation, China. His current research interests include image processing, neural network and pattern recognition.



**Qiwei Xie** received his Ph.D. degree in Data Mining from University of Science and Technology of China, in 2007. He is currently an associate professor in Institute of Automation, Chinese Academy of Sciences. His current research interests include image processing, data mining and pattern recognition.



**Xi Chen** received his B.S. degree in Electronic and Information Engineering from Xi'an Jiaotong University, China, in 2004, and Ph.D. degree in Pattern Recognition and Intelligent Systems from Institute of Automation, Chinese Academy of Sciences, in 2009. He is currently an associate professor in Institute of Automation, Chinese Academy of Sciences. His current research interests include image registration, computational neuroscience and pattern recognition.



**Hua Han** received his Ph.D. degree in Pattern Recognition and Intelligent Systems from Institute of Automation, Chinese Academy of Sciences in 2004. He is currently a professor in Institute of Automation, Chinese Academy of Sciences, a member of CBS Center for Excellence in Brain Science and Intelligence Technology, and a professor in University of Chinese Academy of Sciences. His current research interests include image processing, computational neuroscience and pattern recognition.